

Article

Hydraulic Travel Time Diagnosis Using Recovery Data from Short-Term Pumping Tests for Rapid Aquifer Characterization: A Numerical Study with Monte-Carlo Simulations

Junjie Qi ¹, Rui Hu ^{1,*}, Linwei Hu ², Quan Liu ³, Xiaolan Hou ¹ and Yang Song ¹

¹ School of Earth Science and Engineering, Hohai University, Fo Cheng Xi Road 8, Nanjing 211100, China; hhqjunjie@hotmail.com (J.Q.); hou_xl@hhu.edu.cn (X.H.); soongyaung@hhu.edu.cn (Y.S.)

² Institute of Geosciences, Kiel University, 24118 Kiel, Germany; linwei.hu@ifg.uni-kiel.de

³ Geoscience Center, University of Göttingen, 37077 Göttingen, Germany; quan.liu@uni-goettingen.de

* Correspondence: rhu@hhu.edu.cn

Abstract: In the realm of groundwater science, characterization of heterogeneous aquifers is pivotal for resolving diverse groundwater resource and engineering-related problems that require the detailed spatial distribution of hydraulic parameters. As research progresses, one hydraulic tomographical method, which is based on hydraulic travel time inversion, emerges as a promising and rapid method due to its robust and efficient calculation. In the field, the acquisition of hydraulic excitation and head observation data required for inversion is less time-consuming. Data collection from a single hydraulic test (such as a pumping test) typically takes only a few minutes or even a few tens of seconds. However, the field application of this method faces challenges. Hydraulic travel time is typically generated in the early stages of hydrogeological tests (e.g., early drawdown of a pumping test), yet accurate data may not be readily available because of the noise signals from test equipment, which can contaminate travel time signals, leading to inaccurate inversion results. A potential solution lies in utilizing the smooth head observation during the recovery period after the pump is turned off, which yields more accurate travel times for inversion calculations. In this paper, the mathematical development suggests that the travel time of the recovery phase aligns with that of the pumping phase when pumping reaches a steady or quasi-steady state. Subsequently, by employing Monte-Carlo simulations, 1200 realizations of two-dimensional heterogeneous confined aquifer models were generated for simulating pumping tests with different pumping durations. The calculated head data were then utilized to compute the travel time derived from drawdown data (t) and recovery data (t'), respectively. Comparisons showed that t is equal to t' when drawdown reaches a steady or quasi-steady state. Conversely, when the pump is turned off before reaching a quasi-steady state, t differs from t' . However, results also indicate the fact that a decent hydraulic travel time diagnosis can be obtained, especially for the cases when travel times are smaller than 15 s. Given the statistical results of Monte-Carlo simulations, as well as experience during pumping tests in the field with different scenarios, using the recovery data from 60 s of pumping duration, or extended pumping durations of 100 s or 200 s as a more conservative alternative, can replace the aquifer characterization based on drawdown data. The new inversion strategy not only has less data uncertainty and equivalent inversion accuracy, but also can greatly enhance the repeatability of field tests and reduce the environmental impact of long-term pumping tests.



Citation: Qi, J.; Hu, R.; Hu, L.; Liu, Q.; Hou, X.; Song, Y. Hydraulic Travel Time Diagnosis Using Recovery Data from Short-Term Pumping Tests for Rapid Aquifer Characterization: A Numerical Study with Monte-Carlo Simulations. *Water* **2024**, *16*, 1677. <https://doi.org/10.3390/w16121677>

Academic Editor: Yeshuang Xu

Received: 3 May 2024

Revised: 28 May 2024

Accepted: 11 June 2024

Published: 12 June 2024



Copyright: © 2024 by the authors. Licensee MDPI, Basel, Switzerland. This article is an open access article distributed under the terms and conditions of the Creative Commons Attribution (CC BY) license (<https://creativecommons.org/licenses/by/4.0/>).

Keywords: aquifer characterization; hydraulic tomography; hydraulic travel time; pumping test; head recovery; Monte-Carlo simulations

1. Introduction

Groundwater is an invaluable resource essential for various aspects of human life, ranging from daily domestic use to industrial and agricultural development. Within the realm of groundwater science there is a pressing need to utilize groundwater resources

optimally while mitigating the risk of depletion. Furthermore, under certain circumstances, groundwater can pose threats to mining operations, as well as the stability of excavations and dams, while also potentially leading to secondary salinization and waterlogging of soil [1–5]. Accurate and quantitative prediction and management of these challenges necessitate the establishment of a bridge between real-world issues and abstract mathematical problems, which can be achieved through mathematical modeling. However, constructing a reliable model hinges on precise aquifer characterization [6]. In essence, acquiring main hydraulic parameters, including hydraulic conductivity (K), specific storage (S_S), and their ratio, hydraulic diffusivity (D), serves as a vital foundation for the development of effective models to solve groundwater problems.

Numerous methods have emerged to characterize aquifers. Laboratory techniques, such as particle size analysis [7] and permeability tests [8], as well as sampling analysis [9], offer insights and details at a very localized scale. Tests like dipole-flow tests [10], borehole flowmeter tests [11], and multilevel slug tests [12] can provide vertical profiles of K , albeit within a constrained range. Tracer tests [13], although offering extensive coverage, are time-intensive and entail injecting substantial volumes of brine, posing environmental concerns. Geophysical methods, notably conductivity logging [14], are commonly employed to assess aquifer heterogeneity. However, conductivity logging lacks a definitive correlation with permeability coefficients, precluding direct determination of hydraulic parameters. Traditional hydrogeological tests [15], such as pumping tests, can provide estimates of hydraulic parameters over larger areas, without the detailed results of parameter distribution. Using inversion techniques in geophysical methods like geo-radar [16], artificial seismic [17], and electrical resistivity surveys [18], the aquifer can be characterized spatially over a larger area. However, the relationship between geophysical parameters (e.g., seismic wave velocity, electrical resistivity) and hydraulic parameters is commonly site-specific and remains inadequately quantified.

Hydraulic tomography (HT) has emerged as a dependable method for effectively characterizing the heterogeneous hydraulic parameters of aquifers in recent years [19–23]. Typically, this method involves two key steps: cross-well pumping tests, and inversion of hydraulic signals to achieve hydraulic parameters. Through inversion techniques, HT enables the reconstruction of high-resolution spatial distribution information regarding heterogeneous hydraulic parameters from extensive hydraulic datasets. The reliability of the method has been substantiated through numerous laboratory and field experiments [24–29].

Inversion methods employed in HT are broadly categorized into two main categories. The first category revolves around groundwater modeling and parameter evaluation. For instance, methodologies like the Continuous Linear Estimation (SLE) algorithm [30,31], the Steady Shape Inversion method [32], and the pilot-point method [33,34] are utilized in parameter evaluation.

The second category is grounded on groundwater travel time inversion, akin to seismic wave travel time inversion in geophysics [32,35–40]. Its distinguishing characteristic lies in the incorporation of the time integral of pressure pulse propagation time, which correlates with the ratio of the square root of peak time of the pressure pulse to the square root of the hydraulic diffusivity. In this approach, the parabolic partial differential equations governing groundwater dynamics are approximated and substituted with hyperbolic equations. These equations are then integrated with the eikonal equation, ultimately transforming into a one-dimensional linear integral along the shortest path of the pressure travel time signal, which significantly enhances the numerical computational efficiency of the method. After years of development, this category of inversion methods possesses a notable advantage compared to the first category: acquisition of the hydraulic excitation and observation data required for inversion is less time-consuming. Data collection from a single hydraulic test (such as a pumping test) typically takes only a few minutes or even a few tens of seconds. Inversion calculations are also less time-consuming. Experience has shown that it takes only tens of seconds to generate a 2D or 3D tomogram using a standard computer [32].

The resolution of the tomogram, however, depends on the size of the field domain and the quantity of source-receiver pairs.

When applying hydraulic-travel-time-based methods, an accurate determination of hydraulic travel time is crucially important, i.e., the actual time length between the beginning of drawdown in the pumping well and the peak time point in the observation wells. As shown in Figure 1, a common challenge arises due to the early appearance of noise signals during the pumping process. This can lead to inaccurate time calculations, not only for the time where the drawdown starts, but also for the peak time. While denoising techniques are often employed to mitigate this issue, they can introduce errors that impact the accuracy of inversion calculations [37]. During experimentation, it has been observed that, after pumping ceases, groundwater levels recover, resulting in a smoother head recovery curve in wells compared to the drawdown curves [41]. Furthermore, it has been noted that noise from pumps and other equipment is largely eliminated during this recovery phase. As a result, a key question arises regarding whether to utilize the time signal during the water level recovery phase for hydraulic time inversion. This decision, along with determining the time to cease pumping, is crucial for efficiently and accurately characterizing the heterogeneous structure of the aquifer.

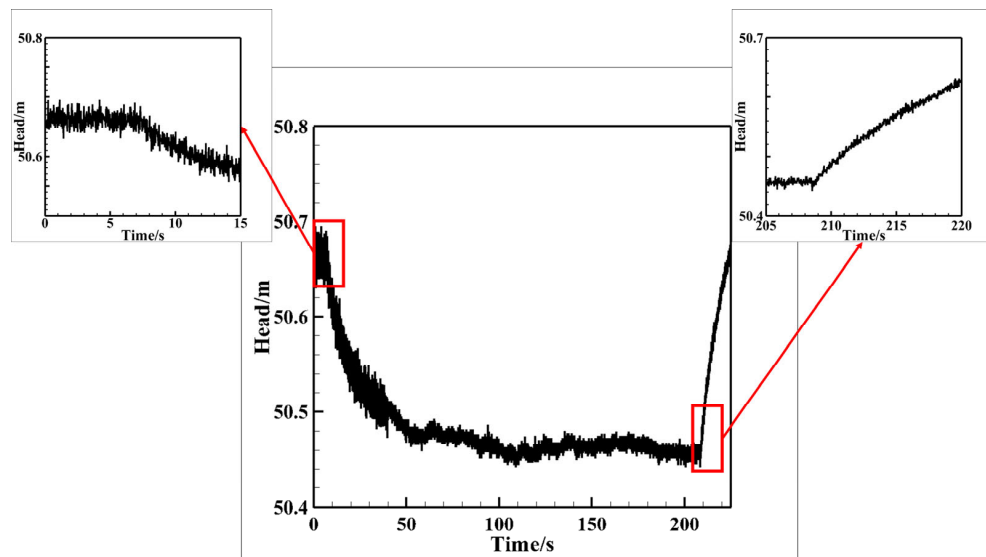


Figure 1. Noise-containing head data of a field pumping test.

2. Methods

2.1. Groundwater Flow Equation and Hydraulic Travel Time for Recovery Tests

The governing equation describing the radial groundwater flow during a pumping test in a homogeneous and isotropic aquifer is written as:

$$K \frac{\partial^2 H}{\partial r^2} + Q(r_p, t) = S_s \frac{\partial H}{\partial t} \quad (1)$$

where K and S_s are the hydraulic conductivity and specific storage, respectively. H is the water head and $Q(r_p, t)$ is the pumping rate per unit volume at location $r = r_p$. Referring to Zhu and Yeh (2006) [41], Equation (1) can be transferred to the following equation for describing drawdown evolution:

$$K \frac{\partial^2 s}{\partial r^2} + K \frac{\partial^2 H_0}{\partial r^2} + Q(r_p, t) = S_s \frac{\partial s}{\partial t} \quad (2)$$

where $s = H - H_0$ is the drawdown, and H_0 is the initial water head. The second term in Equation (2), $K \frac{\partial^2 H_0}{\partial r^2}$, shows the divergence flow field before pumping starts, and equals

zero in the case where the initial head distribution is in a steady or quasi-steady state. Therefore, Equation (2) can be reformulated as:

$$D \frac{\partial^2 s}{\partial r^2} + Q(r_p, t) = \frac{\partial s}{\partial t} \quad (3)$$

where $D = \frac{K}{S_s}$ is the hydraulic diffusivity. In the case where the pumping rate Q is a constant over time (i.e., a Heaviside pulse) and the initial drawdown is zero, the solution of Equation (3) in an infinite domain was given by Häfner et al. [42]:

$$s_{pump}(r, t) = \frac{Q}{4\pi r K} erfc \frac{r}{\sqrt{(4Dt)}} \quad (4)$$

where s_{pump} is the drawdown during pumping. t indicates the time after pumping starts. To derive the hydraulic travel time, the first and second temporal derivative of s_{pump} are calculated through:

$$\frac{ds_{pump}}{dt} = \frac{Q}{\sqrt{(4\pi Kt)^3 / S}} \exp\left(-\frac{r^2}{4Dt}\right) \quad (5)$$

$$\frac{d^2 s_{pump}}{dt^2} = \left[-\frac{1.5Q}{\sqrt{(4\pi Kt)^3 t^5 / S}} + \frac{Q}{\sqrt{(4\pi Kt)^3 / S}} \left(\frac{r^2}{4Dt^2} \right) \right] \exp\left(-\frac{r^2}{4Dt}\right) \quad (6)$$

The maximum value of $\frac{ds_{pump}}{dt}$ appears when $\frac{d^2 s_{pump}}{dt^2}$ equals zero. To fulfil this condition, t equals $\frac{r^2}{6D}$, which is called the hydraulic travel time.

Now we consider the drawdown during the recovery period (s_{rec}). By applying the superposition principle, s_{rec} can be defined as the summation of two pumping tests:

$$s_{rec}(r, t') = s_{pump1}(r, t) + s_{pump2}(r, t') \\ = \frac{Q}{4\pi r K} erfc \frac{r}{\sqrt{4D(t_p + t')}} - \frac{Q}{4\pi r K} erfc \frac{r}{\sqrt{4Dt'}} \quad (7)$$

where s_{pump1} is the drawdown of a pumping test at a constant rate of Q , and s_{pump2} is the drawdown of an imaginary test at a constant rate of $-Q$. t_p is the time at which pumping suspends. t' is the time after the pump is turned off. Hence, $t = t' + t_p$.

2.1.1. Pumping Reaches a Steady State or Approximate Steady State

The steady state or approximate steady state condition implies that the change in drawdown along with the time at all observation locations is zero or nearly zero, respectively. Therefore, in the case where pumping reaches a steady/approximate steady state, the first temporal derivative of $s_{pump1}(r, t)$ equals zero:

$$\frac{ds_{rec}}{dt'} = \frac{ds_{pump2}}{dt'} = -\frac{Q}{\sqrt{(4\pi Kt')^3 / S}} \exp\left(-\frac{r^2}{4Dt'}\right) = -\frac{ds_{pump}}{dt} \quad (8)$$

When $t' = \frac{r^2}{6D}$, the minimum value of the first temporal derivative $\left(\frac{ds_{rec}}{dt'}\right)_{min}$ equals $-\left(\frac{ds_{pump}}{dt'}\right)_{max}$, which equals $-\frac{Q}{\sqrt{\left(\frac{2\pi}{3}\right)^3 S r^3}} \exp\left(-\frac{3}{2}\right)$.

2.1.2. Pumping Reaches a Quasi-Steady State

In the real world, a steady state condition might be difficult to reach because flow boundaries are too far or not explicit. Moreover, it might require a sufficiently long time to achieve the approximate steady state condition. On the contrary, a quasi-steady state could be established much faster than an approximate steady state condition.

The first temporal derivative of $s_{rec}(r, t')$ is:

$$\frac{ds_{rec}}{dt'} = \frac{Q}{\sqrt{[4\pi K(t_p + t')]^3/S}} \exp\left[-\frac{r^2}{4D(t_p + t')}\right] + \frac{Q}{\sqrt{(4\pi Kt')^3/S}} \exp\left(-\frac{r^2}{4Dt'}\right) \quad (9)$$

A quasi-steady state condition is established, as the relative change in $\frac{ds_{pump}}{dt}$ is smaller than 1% (Zha et al. [43]). In this case, we consider the first term of the right-hand part in Equation (9) approximately equals a constant value of $\frac{Q}{\sqrt{(4\pi Kt_p)^3/S}} \exp\left[-\frac{r^2}{4Dt_p}\right]$. Then, the second temporal derivative of s_{rec} is formulated as:

$$\frac{d^2s_{rec}}{dt'^2} = \left[1.5 \frac{Q}{\sqrt{(4\pi K)^3 t'^5 / S_s}} - \frac{Q}{\sqrt{(4\pi Kt')^3 / S_s}} \frac{r^2}{4Dt'^2} \right] \exp\left(-\frac{r^2}{4Dt'}\right) \quad (10)$$

The minimum $\left(\frac{ds_{rec}}{dt'}\right)_{min}$ appears when $t' = \frac{r^2}{6D}$, which is the same as the travel time during the pumping test.

Comparison of Equations (5), (8) and (9) indicates that the early diagnostics of recovery tests are equivalent to those of pumping tests, if pumping reaches a steady-state, approximate steady state, or quasi-steady state.

In the derivation of the analytical solution, the second temporal derivative of s is used to determine the maximum and minimum values of the first temporal derivative of s , while for the head time data obtained from pumping tests, the time corresponding to its maximum value, i.e., the travel time, is found by taking its first-order derivative.

2.2. Monte-Carlo Simulations

The spatial distribution of parameters, such as K , and S_s , remains unknown in most aquifer systems. One approach to address this uncertainty is to treat these parameters as random variables characterized by their probability density distributions. Consequently, a heterogeneous aquifer can be viewed as a system composed of numerous spatially distributed random variables, forming a random field with multiple possible parameter fields (realizations). A joint probability distribution is then used to describe the likelihood of a specific realization occurring. Because geological deposition processes may lead to spatial correlations between parameters at different locations, the joint probability distribution needs to consider an autocorrelation function, along with mean and variance [44,45].

A two-dimensional autocorrelation function is employed as follows:

$$\rho(\xi) = \exp\left\{-\left[\left|\frac{\xi_1}{\lambda_1}\right|^2 + \left|\frac{\xi_2}{\lambda_2}\right|^2\right]^{1/2}\right\} \quad (11)$$

where ξ is the separation vector with components ξ_1 and ξ_2 . λ_1 and λ_2 are correlation lengths in x and y directions, respectively, representing the average dimension (i.e., width, length, and thickness) of the heterogeneity (e.g., stratifications, layers, or clusters).

Given the nature of aquifer heterogeneity, Monte-Carlo simulation (MCS) represents a viable approach to elucidating the most probable aquifer behaviors and their associated uncertainties, as well as examining the relationship between heterogeneity and aquifer responses under specific stress conditions. MCS, while straightforward, is computationally intensive as it involves generating numerous realizations of heterogeneous parameter fields and subsequently simulating aquifer responses. A spectral method [45,46] is usually employed to generate many realizations of the natural logarithms of hydraulic conductivity $\ln(K)$ and specific storage $\ln(S_s)$. These parameters are assumed to follow a normal probability distribution.

3. Numerical Study Based on Monte-Carlo Simulations

In the previous section, the governing equations describing radial groundwater flow in a homogeneous and isotropic aquifer were examined. It was deduced that the early diagnostics of recovery tests are equivalent to those of pumping tests, if pumping reaches a steady-state, approximate steady state, or quasi-steady state. Nonetheless, in practice, the spatial arrangement of pertinent aquifer parameters remains undisclosed. The Monte-Carlo method, renowned for its stochastic simulation capabilities, offers a viable approach. It treats the unidentified parameters at each location as stochastic variables, characterized by their probability density distributions. Through an extensive series of simulations, this method unveils discernible trends. This chapter aims to construct a series of random models featuring diverse parameter distributions to illustrate how the conclusions derived from the previous chapter behave in heterogeneous models by employing Monte-Carlo simulations.

3.1. Model Set Up

A series of confined, saturated, two-dimensional heterogeneous aquifer models were randomly generated using VSAFT2 (Variably Saturated Flow and Transport utilizing the Modified Method of Characteristics, in 2D), which is intensively applied for the synthetic model building, random field generation, and forward simulation. The VSAFT2 program was developed by Yeh's group [47], and is available via <http://tian.hwr.arizona.edu/downloads/> (accessed on 3 May 2024). To facilitate the verification of the conclusions from the previous chapter, the models were established with parameter settings as follows, which enabled reaching a steady state relatively quickly and allowed for efficient observation of changes in travel time. The model size was set to $20 \text{ m} \times 10 \text{ m}$. The grid size was 20 rows and 40 columns, with each grid cell measuring 0.5 m. Figure 2a shows the model geometry, meshing, and boundary settings. The left and right boundaries were set as constant head boundaries, maintained at a value of 100 m. The upper and lower boundaries were established as no-flow boundaries to replicate the confined condition. The initial head was uniformly set to 100 m across all grid cells and the porosity was set to 0.4. The specific parameters are illustrated in Table 1; the mean and variance of $\ln(K)$ were set as -12 m/s and 1 m/s , and the mean and variance of $\ln(S_S)$ are -12 m^{-1} and 1 m^{-1} . The mean and variance were calculated by the mean and variance of $\ln(K)$ and $\ln(S_S)$. A series of realizations of random fields of $\ln(K)$ and $\ln(S_S)$, with given means (-12 m/s and -12 m^{-1}), variances (1 m/s and 1 m^{-1}), and correlation lengths ($\lambda_x = \lambda_y = 20 \text{ m}$), were generated using a spectral method (introduced in Section 2.2). Figure 2b,c show one realization of the K field and S_S field, respectively. Afterward, with each pair of K field and S_S field, corresponding head data changing with time in the observation well can be obtained by a transient forward simulation of pumping at the pumping well using VSAFT2. Two wells were positioned within the model: a pumping well, PW (located at $x = 7 \text{ m}$, $y = 5 \text{ m}$; the red circle at Figure 2a), and an observation well, OW (located at $x = 13 \text{ m}$, $y = 5 \text{ m}$; the blue circle at Figure 2a), with a pumping rate of $0.0001 \text{ m}^3/\text{s}$. Afterwards, with each pair of K field and S_S field, corresponding temporal head data in the observation well can be obtained by a forward simulation of the transient pumping test at the pumping well.

Table 1. Parameters set in the simulated model.

Parameter	Mean (\ln)	Variance (\ln)	Mean	Variance
K	-12	1	$1.01300939 \times 10^{-5}$	$1.76328022 \times 10^{-10}$
S_S	-12	1	$1.01300939 \times 10^{-5}$	$1.76328022 \times 10^{-10}$

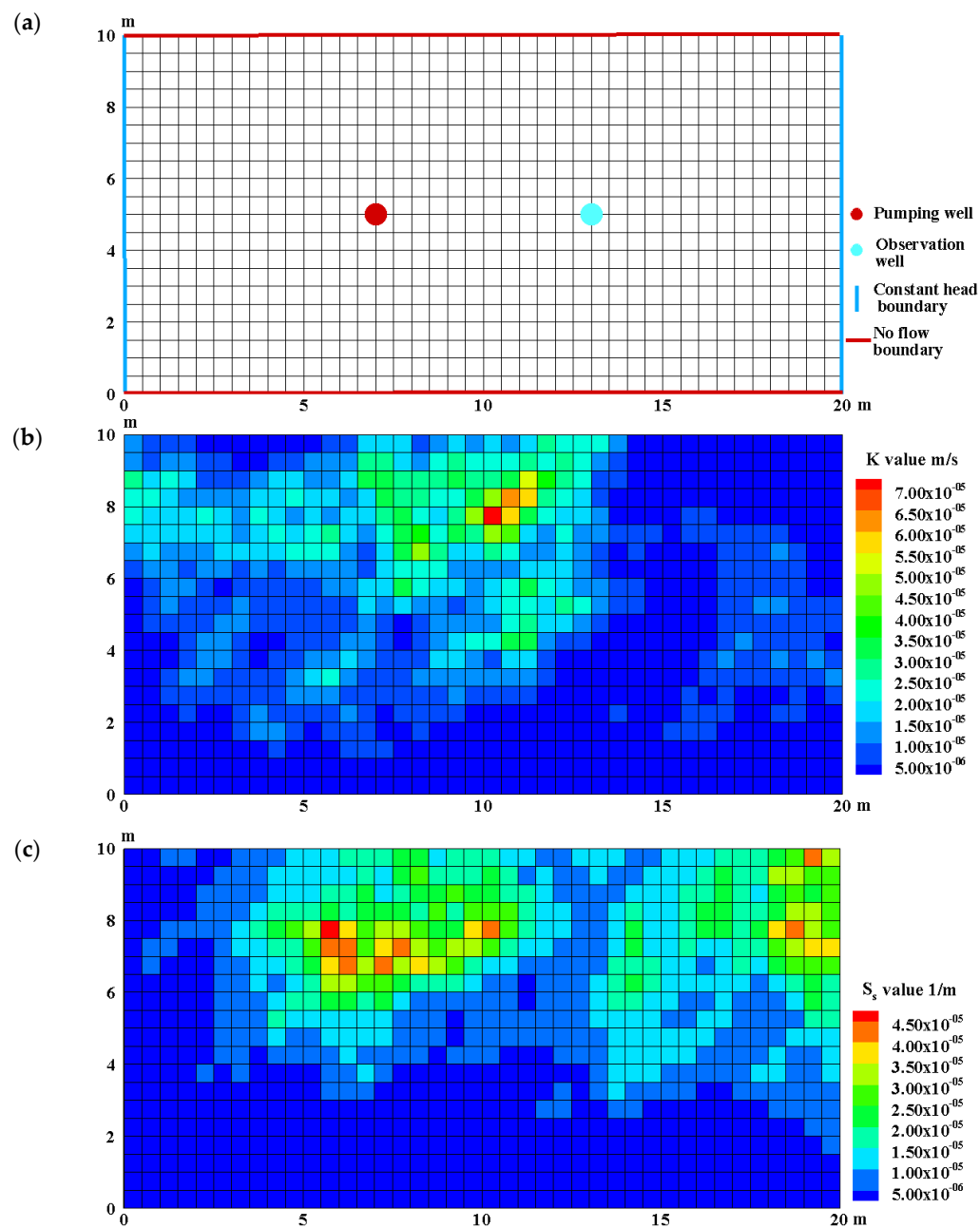


Figure 2. (a) The synthetic aquifer model: blue and red circles represent the observation well and pumping well, respectively. (b) one realization of K field, and (c) one realization of S_s field.

3.2. General Pumping Tests

Monte-Carlo simulations of a pumping test were first carried out in this section, spanning a total duration of 1000 s, with 800 s dedicated to pumping and 200 s for recovery. The time step was 0.5 s, resulting in a total of 2000 steps. MCS yielded representative measurements 200 times, which are introduced in detail in Section 3.4. After performing the MCS, the average drawdown of the observation well during the pumping period was calculated and is plotted in Figure 3. It can be observed that after 600 s, the water level stabilizes. Hence, it can be inferred that 800 s of pumping time is sufficient to reach the steady state of the pumping test. This experiment aims to determine whether the hydraulic travel time of the recovery period can substitute for the pumping period when the pumping reaches the steady state, and also to provide insights for the design of subsequent tests.

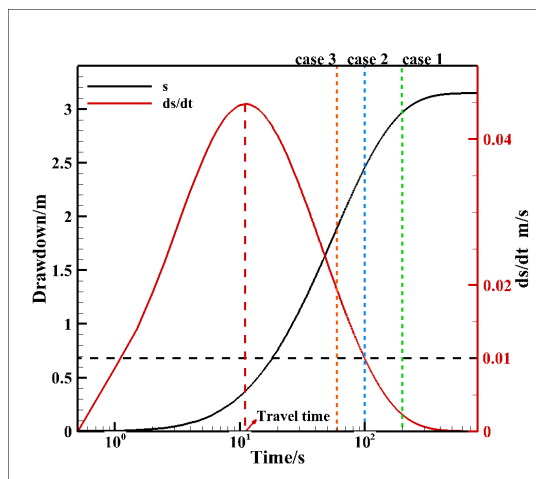


Figure 3. General pumping test mean drawdown and its first order derivatives. (The red dashed line refers to the definition of travel time mentioned in Section 1. The orange, blue and green dashed lines indicate the selected three cases of short-time pumping tests. And the black dashed line indicates where the value of first order derivatives of drawdown equals 0.01).

3.3. Short-Term Pumping Tests

In the real world, a steady state condition might be difficult to reach because the flow boundaries are too far or not explicit. Moreover, it might require a sufficiently long time to achieve the approximate steady state condition. Additionally, limited test time can sometimes pose an additional challenge in achieving a steady state during the pumping test. On the contrary, a quasi-steady state could be established much faster than an approximate steady state condition. A quasi-steady state condition was established, as the relative change in $\frac{ds_{\text{pump}}}{dt}$ was smaller than 1% [43]. The red line in Figure 3 depicts the first-order derivative of the average drawdown during the pumping tests conducted at 200 sites, while the black dashed line indicates the scenario where $\frac{ds_{\text{pump}}}{dt}$ equals 0.01. The intersection of the dashed line and the red line represents the average quasi-steady time across 200 simulated general pumping tests, which is 100 s. Hence, three pumping scenarios, which were pumping times of 200 s (greater than the average quasi-steady time), 100 s (equal to the average quasi-steady time), and 60 s (less than the average quasi-steady time), were designed (the vertical dashed line in Figure 3):

Case 1: Monte-Carlo simulations for a short-term pumping test, conducted over a total duration of 400 s, comprising 200 s of pumping time and 200 s of recovery, with a time step of 0.2 s, leading to a total of 2000 steps. The sample size of the MCS was 200.

Case 2: Monte-Carlo simulations for a short-term pumping test, conducted over a total duration of 200 s, comprising 100 s of pumping and 100 s of recovery, with a time step of 0.2 s, leading to a total of 1000 steps. The sample size of the MCS was 200.

Case 3: Monte-Carlo simulations for a short-term pumping test, conducted over a total duration of 120 s, comprising 60 s of pumping time and 60 s of recovery, with a time step of 0.2 s, leading to a total of 600 steps. The sample size of the MCS was also 200.

The simulated head data in each MCS were then utilized to compute the first-order derivatives, facilitating the calculation of travel times for both the drawdown period and the subsequent recovery period.

3.4. Stability of Monte-Carlo Simulations

To ensure the convergence of Monte-Carlo simulations in yielding representative measurements, it is imperative to observe a stabilization in the average head value at specific time points in the observation wells as the number of simulations increases. In the general case, i.e., the pumping test simulations introduced in Section 3.2, the head data from 200 realizations at 5 s, 100 s, 400 s, 805 s, and 900 s were selected (Figure 4a). For

Case 1, the head data from 200 realizations at 5 s, 100 s, 205 s, and 300 s were selected (Figure 4b). For Case 2, the head data from 200 realizations at 5 s, 80 s, 105 s, and 180 s were selected (Figure 4c), and for Case 3, the head data from 200 realizations at 5 s, 50 s, 65 s, and 100 s were selected (Figure 4d). These time selections encompass early, middle, and late periods of pumping, as well as early, middle, and late periods of recovery, to ensure the representativeness.

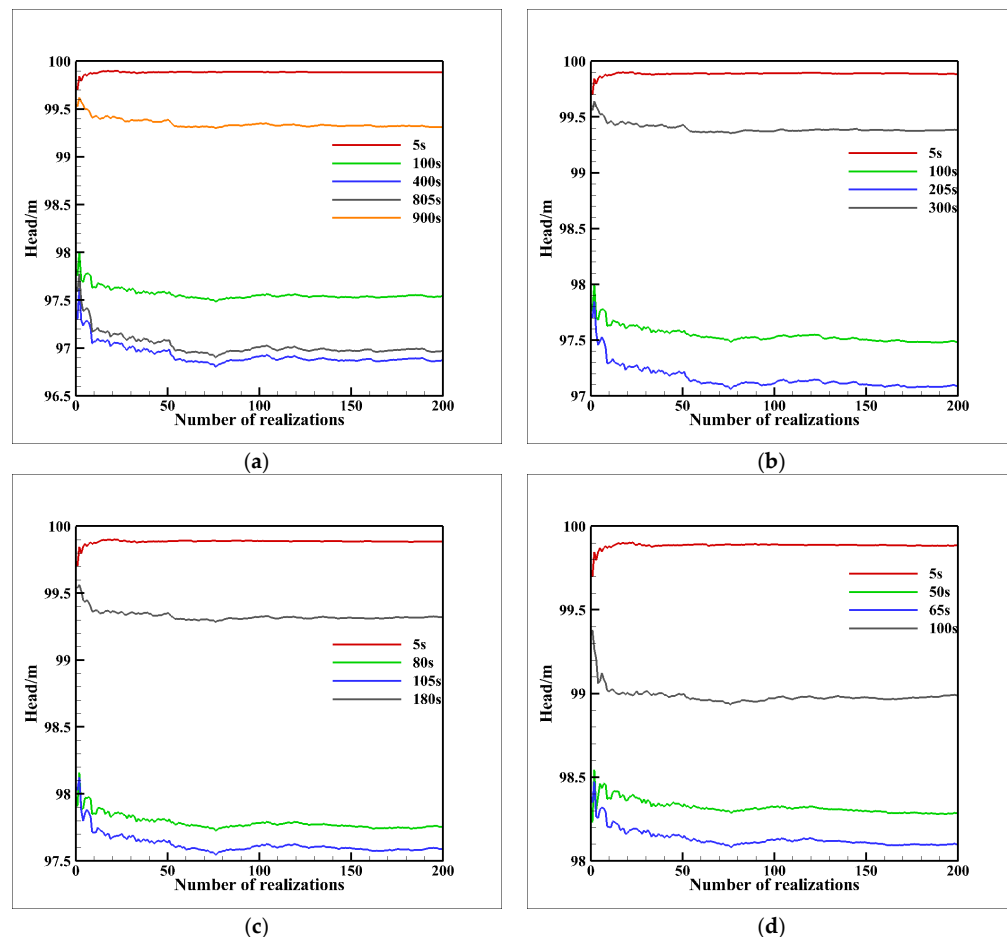


Figure 4. Head in the observation well at different times as a function of the number of realizations for pumping tests simulation. (a) General case, (b) Case 1, (c) Case 2 and (d) Case 3.

Analysis of the results shown in Figure 4 reveals that in the initial 20 simulations of all cases, the head in the observation wells exhibited significant fluctuations. However, as the number of simulations increased, these fluctuations gradually diminished and approached stability, reaching a plateau after approximately 150 simulations. This trend indicates the credibility and representativeness of the conclusions derived from the Monte-Carlo simulations.

4. Result and Discussion

4.1. Result Comparison of the General Case and Three Cases

The head observation curves and the scatter plots depicting the travel time derived from drawdown (t) and recovery (t') periods from the general case (Section 3.2) and the three other cases (Section 3.3) with short-term pumping are presented below:

For the general pumping tests with drawdown reaching a steady state, it is obvious that all black dots are located on the red line, that is, the travel time of water level recovery is equal to that of drawdown (Figure 5b).

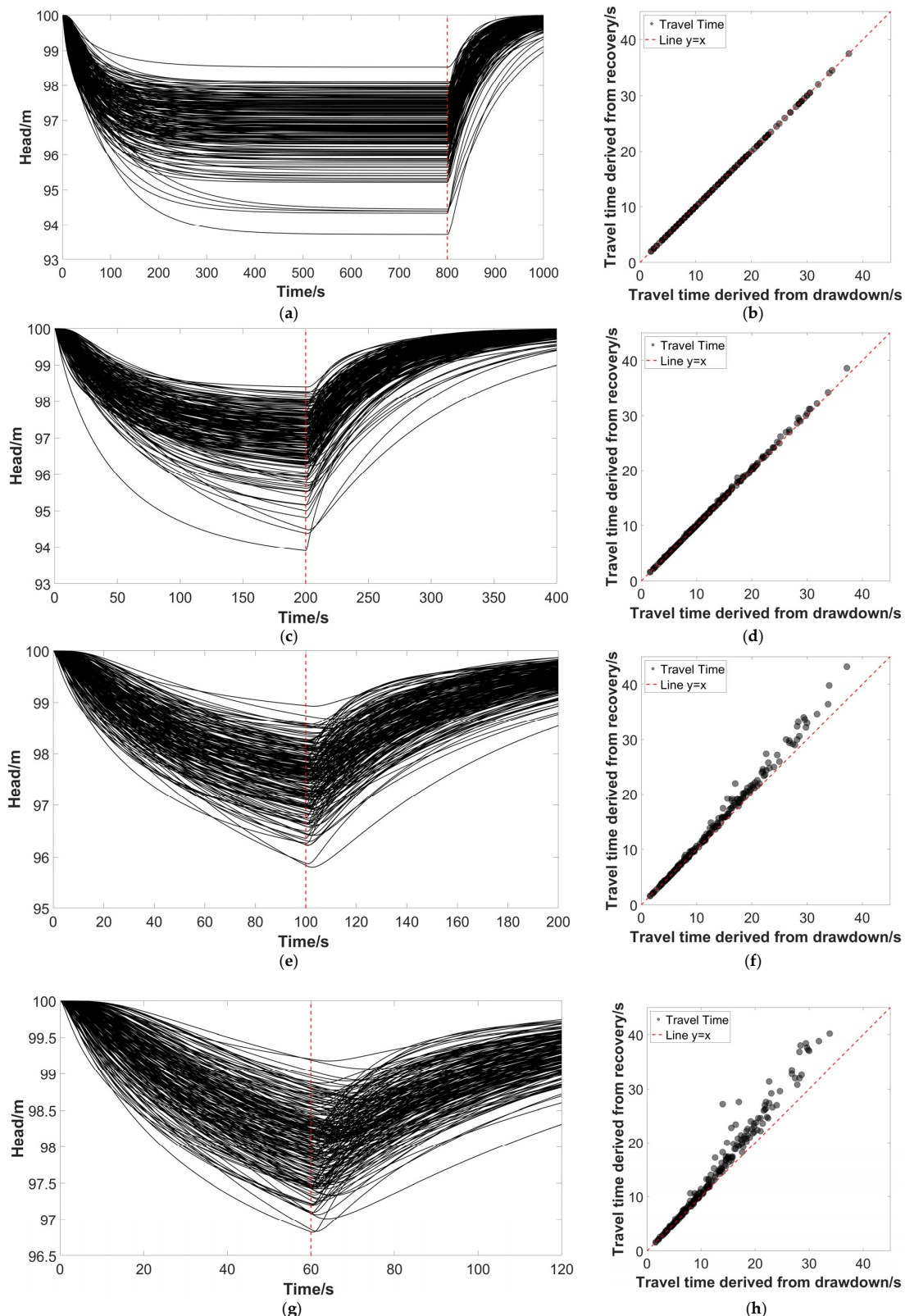


Figure 5. (a) Head observation for the pumping tests with drawdown reaching a steady state; (b) t vs. t' derived from the head data of (a); (c) head observation of the pumping tests in Case 1; (d) t vs. t' for case 1; (e) head observation for the pumping tests in Case 2; (f) t vs. t' for Case 2; (g) head observation for the pumping tests in Case 3; (h) t vs. t' for Case 3. (The red dashed lines in (a,c,e,g) indicate the cessation times of pumping for their corresponding cases).

Conversely, in the cases of short-term pumping tests, some of the black dots are located above the red line, that is, t appears slightly longer than t' . For Case 1, most black dots align with the red line, indicating that although the pumping test has not yet reached a steady state, in terms of the travel time diagnosis, t' closely resembles t . For Case 2, when the travel time exceeds approximately 20 s, the black dots deviate further from the red line. This suggests a greater disparity between t and t' . Furthermore, for Case 3, when the travel time exceeds approximately 15 s, the black dots notably diverge from the red line, highlighting a significant variance in t and t' . Additionally, from some head diagrams in Figure 5c,e,g, it can be observed that the head continues to decrease after pumping cessation, indicating a lag in t' .

Considering that the pumping durations of Cases 1–3 (200 s, 100 s and 60 s) were set based on the average quasi-state time (100 s), it is important to note that the quasi-state time varies for each pumping test in each realization. This results in most realizations of Case 1 having a quasi-state time less than 200 s. Therefore, travel time diagnosis in Case 1 is most appropriate, which means the black dots deviate slightly. In contrast, for Case 3, the approximate stabilization time for most sites exceeds 60 s. Consequently, the deviation of the black dots is greater compared to that in Cases 1 and 2. Case 2 falls between these extremes. To provide a more intuitive representation of the relationship between the approximate stabilization time and pumping time in Case 2, we selected the drawdown data and their first-order derivatives from five realizations and plotted them in Figure 6. Their t and t' values are listed in Table 2.

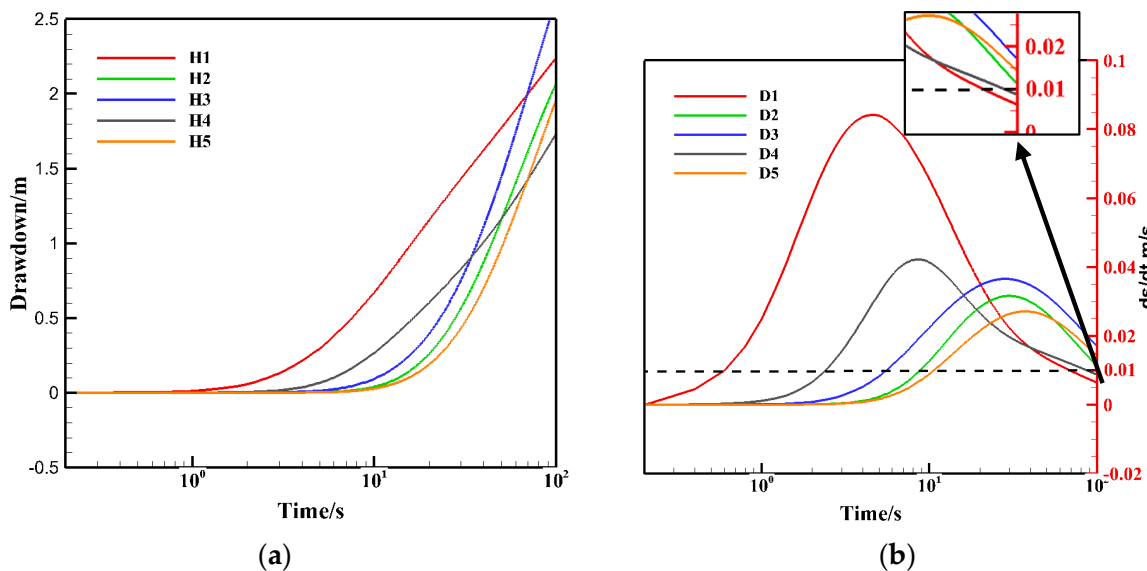


Figure 6. Drawdown data and their first order derivatives from five realizations in Case 2. (a) drawdown data and (b) first order derivatives.

Table 2. Travel time derived from drawdown and recovery from five realizations in Case 2.

Realizations	1	2	3	4	5
Color	Red	Green	Blue	Grey	Orange
Travel time derived from drawdown data (t , seconds)	4.6	30	28.4	8.6	37.2
Travel time derived from recovery data (t' , seconds)	4.6	33	29.6	8.6	43.2

From Table 2, it can be observed that t' in realizations 1 and 4 is equal to t . Figure 6b shows that at 100 s, the red and grey lines are below the black dashed line, which means that $\frac{ds_{\text{pump}}}{dt}$ of the two realizations are smaller than 0.01. This indicates that realizations 1

and 4 reached a quasi-steady state condition, resulting in the recovery time equaling the pumping time. Conversely, for realizations 2, 3, and 5, the travel time differs, as indicated by the green, blue, and orange lines lying above the black dashed line (which means that $\frac{ds_{\text{pump}}}{dt}$ values of the three realizations are larger than 0.01). This result further validates the conclusions derived from the formula in Section 2.1.

Upon comparing the variation between t and t' in Figure 5d,f,h, we can recognize on the one hand that the shorter the pumping time and the larger the travel times, the larger the variation will be, especially in cases where the travel times are larger (e.g., larger than 20 s). On the other hand, for the cases when travel times are less than 15 s, even if the pumping duration is only 60 s, t' closely matches t . This is further validated in the next section.

4.2. Hydraulic Travel Time Diagnosis when Pumping Time Is 60 s

Considering the relatively small value of K set in the model, to validate the feasibility of the 60 s pumping scheme for sites with a wider range of hydraulic conductivity, we conducted two further groups of 200 Monte-Carlo simulations by setting the variance of $\ln(K)$ and $\ln(S_S)$ to $3 \text{ m/s}, 3 \text{ m}^{-1}$ and $5 \text{ m/s}, 5 \text{ m}^{-1}$ on top of the original model. Subsequently, we plotted the travel times during the pumping and recovery period as a scatter plot, as shown in Figure 7. Similarly, the head data from 200 realizations at 5 s, 50 s, 65 s, and 100 s were selected to ensure the stability and adequacy of Monte-Carlo simulations, with results shown in Figure 8.

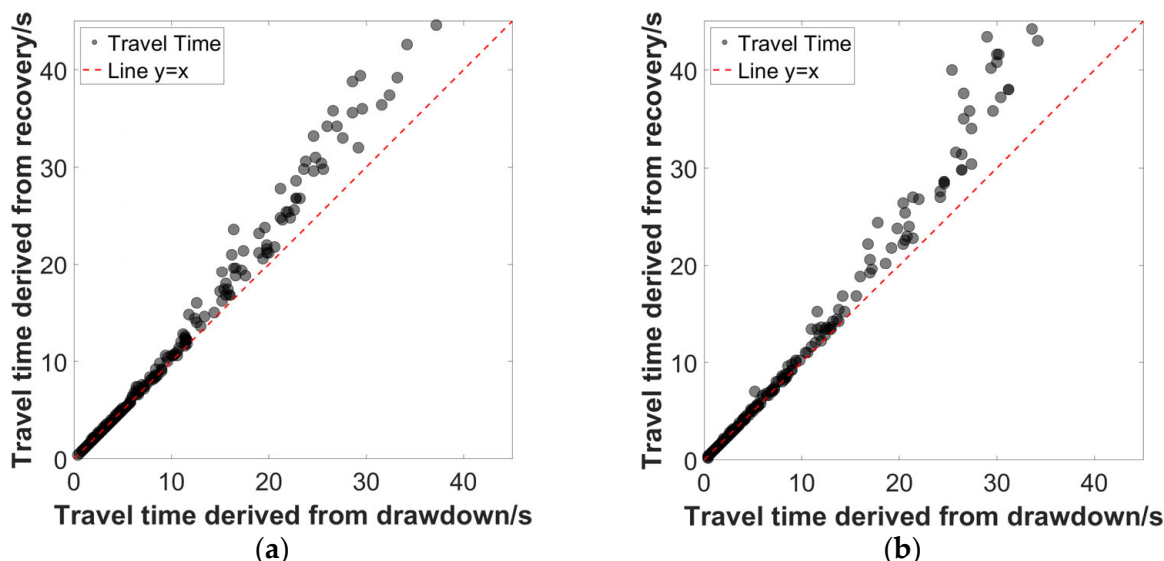


Figure 7. Travel time derived from drawdown (t) and recovery (t') for variance of $\ln(K)$ and $\ln(S_S)$ set to $3 \text{ m/s}, 3 \text{ m}^{-1}$ and $5 \text{ m/s}, 5 \text{ m}^{-1}$. (a) variance set to $3 \text{ m/s}, 3 \text{ m}^{-1}$ and (b) variance set to $5 \text{ m/s}, 5 \text{ m}^{-1}$.

Comparing Figure 7a,b with Figure 5h, it is noticeable that as the variance increases, the range of values for K and S_S also expands, leading to an increase in hydraulic heterogeneity across the model. Despite this, accurate hydraulic travel time diagnoses are still obtained in each case when travel times are less than 10 s. Additionally, the data points are more densely packed or overlapping within the first 10 or 15 s, which visually accounts for the fewer total data points in Figure 7a,b compared to Figure 5h, and indicates the fact that the pumping tests with less than 15 s of travel time are the dominant cases in nature.

Figure 8 shows that after 150 realizations, the observed head at different times no longer changes significantly. As a result, it can be concluded that 200 realizations are sufficient for obtaining representative results.

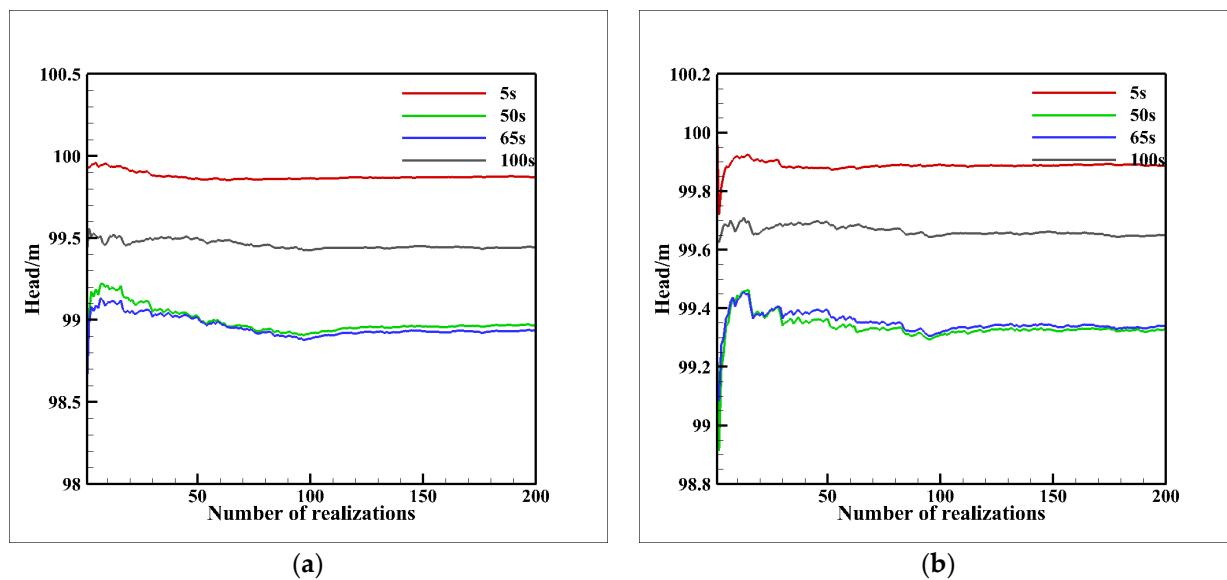


Figure 8. Head in the observation well at different times as a function of the number of realizations for pumping test simulations. (a) variance of $\ln(K)$ and $\ln(S_S)$ set to $3 \text{ m/s}, 3 \text{ m}^{-1}$ and (b) variance of $\ln(K)$ and $\ln(S_S)$ set to $5 \text{ m/s}, 5 \text{ m}^{-1}$.

5. Conclusions

Based on the combination of theoretical derivation and numerical modeling with Monte-Carlo simulations, several significant conclusions have emerged:

The mathematical development of the radial groundwater flow equation in homogeneous isotropic aquifers suggests that the hydraulic travel time derived from the recovery phase (t') aligns with that from the drawdown phase (t) when pumping reaches a steady or quasi-steady state.

In the context of a heterogeneous model, it has been established that for a pumping test, when steady state is achieved, t and t' remain consistent, whereas in scenarios of short-term pumping (where a steady state was not attained), t' appears slightly longer than t . However, for pumping tests with smaller travel times, the disparity between t and t' can be negligible.

Based on the Monte-Carlo simulations and the experience in existing field applications, given the high-speed propagation of head pressure and consequent reduction in travel time, and the pumping tests in practical scenarios with greatest possible aquifer heterogeneity and well construction, the hydraulic travel times are typically less than 10 s [48]. For the utilization of hydraulic tomography based on hydraulic travel time inversion, it is advisable to cease pumping approximately 60 s after the test begins, if necessary (e.g., a limitation due to regulations), or extended pumping durations to 100 s or 200 s as a more conservative alternative for the most accurate achievement of travel time.

The findings presented in this work effectively take full advantage of the noise-free head recovery data from pumping tests to obtain the hydraulic travel times, which successfully reduces the uncertainty of travel time achievement through the down phase with much more data noise. It thus enhances the accuracy of hydraulic travel inversion procedures. The much shorter observation time (e.g., after 60 s of pumping) substantially reduces the time investment and increases the repeatability of tests compared to a conventional pumping strategy, which requires steady state conditions to be achieved. Additionally, it offers an avenue for parameter exploration in areas susceptible to contamination or where prolonged pumping is impractical. By minimizing pumping duration, it is more possible to maintain the original conditions, e.g., the saturated–unsaturated and confined–unconfined conditions of the site. This approach finds broad utility across diverse domains, including geological investigations, groundwater resource management, groundwater reservoir con-

struction, surface water–groundwater interactions, underground pollutant migration, and other emergent research areas.

In this study, only two-dimensional confined aquifers were simulated to validate the method. The performance of the introduced method for unconfined aquifers and three-dimensional aquifers needs to be further validated. In addition, field application of this method faces various challenges, which are not considered in this study, e.g., issues stemming from the well construction, interference of other wells, and geometry of the research profile. Nevertheless, this study theoretically validated the reliability of using head recovery data for determination of hydraulic travel times in heterogeneous aquifers with more efficiency and less data uncertainty. These findings establish a new solution for field applications aimed at characterizing aquifer heterogeneity with hydraulic tomography based on travel time inversion.

Author Contributions: Conceptualization, J.Q. and R.H.; Data curation, J.Q.; Formal analysis, J.Q.; Funding acquisition, R.H.; Methodology, J.Q., R.H., L.H., Q.L. and X.H.; Software, J.Q., X.H. and Y.S.; Supervision, R.H.; Validation, J.Q.; Writing—original draft, J.Q.; Writing—review and editing, R.H., L.H., Q.L., X.H. and Y.S. All authors have read and agreed to the published version of the manuscript.

Funding: This work was supported by National Natural Science Foundation of China (NSFC Grant No. 42372280), “Investigating the permeability loss and the spatial heterogenous permeability change of zero-valent iron permeable reactive barrier for groundwater remediation”.

Data Availability Statement: The data presented in this study are available on request from the corresponding author.

Acknowledgments: L.H. thanks the research support from Kiel University. Q.L. thanks the research support from University of Göttingen. Thanks also for the VSAFT2 software developed by Jim Yeh’s team at the University of Arizona (<http://tian.hwr.arizona.edu/downloads/>, accessed on 1 May 2024).

Conflicts of Interest: The authors declare no conflicts of interest.

References

- Guo, Q.; Shi, X.; Kang, X.; Chang, Y.; Wang, P.; Wu, J. Integrating hydraulic tomography, electrical resistivity tomography, and partitioning interwell tracer test datasets to improve identification of pool-dominated DNAPL source zone architecture. *J. Contam. Hydrol.* **2021**, *241*, 103809. [[CrossRef](#)] [[PubMed](#)]
- Liu, F.; Yeh, T.C.J.; Wang, Y.L.; Hao, Y.H.; Wen, J.C.; Wang, W.K. Characterization of basin-scale aquifer heterogeneity using transient hydraulic tomography with aquifer responses induced by groundwater exploitation reduction. *J. Hydrol.* **2020**, *588*, 125137. [[CrossRef](#)]
- Dong, H.Z.; Li, X.Y.; Yeh, T.C.J.; Ge, J. Diagnosis of concentrated leakage channel embedded in dam base by means of hydraulic tomography. *Bull. Eng. Geol. Environ.* **2020**, *79*, 2871–2881. [[CrossRef](#)]
- Mao, D.Q.; Liu, Z.B.; Wang, W.K.; Li, S.C.; Gao, Y.Q.; Xu, Z.H.; Zhang, C. An application of hydraulic tomography to a deep coal mine: Combining traditional pumping tests with water inrush incidents. *J. Hydrol.* **2018**, *567*, 1–11. [[CrossRef](#)]
- Gao, X.; Yeh, T.C.J.; Yan, E.C.; Wang, W.K.; Cai, J.S.; Liang, Y.; Ge, J.; Qi, Y.M.; Hao, Y.H. Fusion of Hydraulic Tomography and Displacement Back Analysis for Underground Cavern Stability Investigation. *Water Resour. Res.* **2018**, *54*, 8632–8652. [[CrossRef](#)]
- Liedl, R.; Ptak, T. Modelling of diffusion-limited retardation of contaminants in hydraulically and lithologically nonuniform media. *J. Contam. Hydrol.* **2003**, *66*, 239–259. [[CrossRef](#)]
- Alyamani, M.S.; Sen, Z. Determination of hydraulic conductivity from complete grain-size distribution curves. *Groundwater* **1993**, *31*, 551–555. [[CrossRef](#)]
- Kalbus, E.; Reinstorf, F.; Schirmer, M. Measuring methods for groundwater–surface water interactions: A review. *Hydrol. Earth Syst. Sci.* **2006**, *10*, 873–887. [[CrossRef](#)]
- Sundaram, B.; Feitz, A.; Caritat, P.D.; Plazinska, A.; Brodie, R.; Coram, J.; Ransley, T. *Groundwater Sampling and Analysis—A Field Guide*; Geoscience Australia: Canberra, Australia, 2009; Volume 27, p. 104.
- Zlotnik, V.A.; Zurbuchen, B.R. Dipole probe: Design and field applications of a single-borehole device for measurements of vertical variations of hydraulic conductivity. *Groundwater* **1998**, *36*, 884–893. [[CrossRef](#)]
- Bomana, G.K.; Molz, F.J.; Boonec, K.D. Borehole flowmeter application in fluvial sediments: Methodology, results, and assessment. *Groundwater* **1997**, *35*, 443–450. [[CrossRef](#)]
- Butler, J.J., Jr. *The Design, Performance, and Analysis of Slug Tests*; CRC Press: Boca Raton, FL, USA, 2019. [[CrossRef](#)]
- Lee, J.; Kitanidis, P.K. Large-scale hydraulic tomography and joint inversion of head and tracer data using the principal component geostatistical approach (PCGA). *Water Resour. Res.* **2014**, *50*, 5410–5427. [[CrossRef](#)]

14. Goldman, M.; Neubauer, F. Groundwater exploration using integrated geophysical techniques. *Surv. Geophys.* **1994**, *15*, 331–361. [[CrossRef](#)]
15. Butler, J.J. Hydrogeological methods for estimation of spatial variations in hydraulic conductivity. *Hydrogeophysics* **2005**, *50*, 23–58. [[CrossRef](#)]
16. Becht, A.; Tronicke, J.; Appel, E.; Dietrich, P. Inversion strategy in crosshole radar tomography using information of data subsets. *Geophysics* **2004**, *69*, 222–230. [[CrossRef](#)]
17. Hyndman, D.W.; Harris, J.M.; Gorelick, S.M. Coupled seismic and tracer test inversion for aquifer property characterization. *Water Resour. Res.* **1994**, *30*, 1965–1977. [[CrossRef](#)]
18. Kohn, R.V.; Shen, H.; Vogelius, M.S.; Weinstein, M. Cloaking via change of variables in electric impedance tomography. *Inverse Probl.* **2008**, *24*, 015016. [[CrossRef](#)]
19. Zhao, Z.F.; Illman, W.A. Three-dimensional imaging of aquifer and aquitard heterogeneity via transient hydraulic tomography at a highly heterogeneous field site. *J. Hydrol.* **2018**, *559*, 392–410. [[CrossRef](#)]
20. Sanchez-Leon, E.; Leven, C.; Haslauer, C.P.; Cirpka, O.A. Combining 3D Hydraulic Tomography with Tracer Tests for Improved Transport Characterization. *Groundwater* **2016**, *54*, 498–507. [[CrossRef](#)] [[PubMed](#)]
21. Berg, S.J.; Illman, W.A. Comparison of Hydraulic Tomography with Traditional Methods at a Highly Heterogeneous Site. *Groundwater* **2015**, *53*, 71–89. [[CrossRef](#)]
22. Ahmed, A.S.; Jardani, A.; Revil, A.; Dupont, J.P. HT2DINV: A 2D forward and inverse code for steady-state and transient hydraulic tomography problems. *Comput. Geosci.* **2015**, *85*, 36–44. [[CrossRef](#)]
23. Illman, W.A. Hydraulic Tomography Offers Improved Imaging of Heterogeneity in Fractured Rocks. *Groundwater* **2014**, *52*, 659–684. [[CrossRef](#)]
24. Zhao, Z.F.; Illman, W.A. On the importance of considering specific storage heterogeneity in hydraulic tomography: Laboratory sandbox and synthetic studies. *J. Hydrol.* **2021**, *593*, 125874. [[CrossRef](#)]
25. Klepikova, M.; Bixel, B.; Jalali, M. Transient hydraulic tomography approach to characterize main flowpaths and their connectivity in fractured media. *Adv. Water Resour.* **2020**, *136*, 103500. [[CrossRef](#)]
26. Fischer, P.; Jardani, A.; Jourde, H. Hydraulic tomography in coupled discrete-continuum concept to image hydraulic properties of a fractured and karstified aquifer (Lez aquifer, France). *Adv. Water Resour.* **2020**, *137*, 103523. [[CrossRef](#)]
27. Cardiff, M.; Zhou, Y.Q.; Barrash, W.; Kitanidis, P.K. Aquifer Imaging with Oscillatory Hydraulic Tomography: Application at the Field Scale. *Groundwater* **2020**, *58*, 710–722. [[CrossRef](#)]
28. Chen, J.L.; Wen, J.C.; Yeh, T.C.J.; Lin, K.Y.A.; Wang, Y.L.; Huang, S.Y.; Ma, Y.; Yu, C.Y.; Lee, C.H. Reproducibility of hydraulic tomography estimates and their predictions: A two-year case study in Taiwan. *J. Hydrol.* **2019**, *569*, 117–134. [[CrossRef](#)]
29. Hochstetler, D.L.; Barrash, W.; Leven, C.; Cardiff, M.; Chidichimo, F.; Kitanidis, P.K. Hydraulic Tomography: Continuity and Discontinuity of High-K and Low-K Zones. *Groundwater* **2016**, *54*, 171–185. [[CrossRef](#)]
30. Zhu, J.F.; Yeh, T.C.J. Characterization of aquifer heterogeneity using transient hydraulic tomography. *Water Resour. Res.* **2005**, *41*, 7. [[CrossRef](#)]
31. Yeh, T.C.J.; Liu, S.Y. Hydraulic tomography: Development of a new aquifer test method. *Water Resour. Res.* **2000**, *36*, 2095–2105. [[CrossRef](#)]
32. Hu, R.; Brauchler, R.; Herold, M.; Bayer, P. Hydraulic tomography analog outcrop study: Combining travel time and steady shape inversion. *J. Hydrol.* **2011**, *409*, 350–362. [[CrossRef](#)]
33. Poduri, S.; Kambhammettu, B.V.N.P.; Gorugantula, S. A New Randomized Binary Prior Model for Hydraulic Tomography in Fractured Aquifers. *Groundwater* **2021**, *59*, 537–548. [[CrossRef](#)] [[PubMed](#)]
34. Poduri, S.; Kambhammettu, B. On the Performance of Pilot-Point Based Hydraulic Tomography with a Geophysical a Priori Model. *Ground Water* **2021**, *59*, 214–225. [[CrossRef](#)]
35. Brauchler, R.; Cheng, J.T.; Dietrich, P.; Everett, M.; Johnson, B.; Liedl, R.; Sauter, M. An inversion strategy for hydraulic tomography: Coupling travel time and amplitude inversion. *J. Hydrol.* **2007**, *345*, 184–198. [[CrossRef](#)]
36. Vasco, D.; Pride, S.R.; Zahasky, C.; Benson, S.M. Calculating trajectories associated with solute transport in a heterogeneous medium. *Water Resour. Res.* **2018**, *54*, 6890–6908. [[CrossRef](#)]
37. Yang, H.C.; Hu, R.; Qiu, P.X.; Liu, Q.; Xing, Y.X.; Tao, R.; Ptak, T. Application of Wavelet De-Noising for Travel-Time Based Hydraulic Tomography. *Water* **2020**, *12*, 1533. [[CrossRef](#)]
38. Liu, Q.; Hu, L.; Hu, R.; Brauchler, R.; Xing, Y.; Qi, J.; Ptak, T. Characterization of aquifer heterogeneity by tomographic slug test responses considering wellbore effects. *J. Hydrol.* **2023**, *627*, 130472. [[CrossRef](#)]
39. Brauchler, R.; Doetsch, J.; Dietrich, P.; Sauter, M. Derivation of site-specific relationships between hydraulic parameters and p-wave velocities based on hydraulic and seismic tomography. *Water Resour. Res.* **2012**, *48*, 3. [[CrossRef](#)]
40. Song, Y.; Hu, R.; Liu, Q.; Qiu, H.; Hou, X.; Qi, J.; Konadu-Amoah, B. Comparison of hydraulic travel time and attenuation inversions, thermal tracer tomography and geostatistical inversion for aquifer characterization: A numerical study. *Water* **2023**, *15*, 2401. [[CrossRef](#)]
41. Zhu, J.F.; Yeh, T.C.J. Analysis of hydraulic tomography using temporal moments of drawdown recovery data. *Water Resour. Res.* **2006**, *42*, 2. [[CrossRef](#)]
42. Häfner, F.; Sames, D.; Voigt, H.-D. Parameteridentifikation. In *Wärme- Und Stofftransport: Mathematische Methoden*; Springer: Berlin/Heidelberg, Germany, 1992; pp. 546–564.

43. Zha, Y.; Yeh, T.-C.J.; Shi, L.; Huang, S.-Y.; Wang, W.; Wen, J.-C. Quasi-steady state conditions in heterogeneous aquifers during pumping tests. *Adv. Water Resour.* **2017**, *106*, 95–110. [[CrossRef](#)]
44. Yeh, T.-C.; Khaleel, R.; Carroll, K.C. *Flow through Heterogeneous Geologic Media*; Cambridge University Press: Cambridge, UK, 2015.
45. Hou, X.; Hu, R.; Yeh, T.C.J.; Li, Y.; Qi, J.; Song, Y.; Qiu, H. A short-term pumping strategy for hydraulic tomography based on the successive linear estimator. *Water Resour. Res.* **2023**, *59*, e2022WR033831. [[CrossRef](#)]
46. Robin, M.; Gutjahr, A.; Sudicky, E.; Wilson, J. Cross-correlated random field generation with the direct Fourier transform method. *Water Resour. Res.* **1993**, *29*, 2385–2397. [[CrossRef](#)]
47. Yeh, T.; Srivastava, R. *VSAFT2: Variably Saturated Flow and Transport in 2-Dimensions, A Finite Element Simulation*; Department of Hydrology and Water Resources, University of Arizona: Tucson, AZ, USA, 1990.
48. Brauchler, R.; Hu, R.; Dietrich, P.; Sauter, M. A field assessment of high-resolution aquifer characterization based on hydraulic travel time and hydraulic attenuation tomography. *Water Resour. Res.* **2011**, *47*, 3. [[CrossRef](#)]

Disclaimer/Publisher’s Note: The statements, opinions and data contained in all publications are solely those of the individual author(s) and contributor(s) and not of MDPI and/or the editor(s). MDPI and/or the editor(s) disclaim responsibility for any injury to people or property resulting from any ideas, methods, instructions or products referred to in the content.